



Wave propagation in one-dimensional fluid-saturated porous phononic crystals with partial-open pore interfaces

Shu-Yan Zhang^a, Dong-Jia Yan^{a,b}, Yue-Sheng Wang^{a,c,*}, Yan-Feng Wang^{c,**}, Vincent Laude^d

^a Institute of Engineering Mechanics, Beijing Jiaotong University, 100044 Beijing, China

^b Applied Mechanics Laboratory, Department of Engineering Mechanics; Center for Flexible Electronics Technology, Tsinghua University, Beijing 100084, China

^c Department of Mechanics, School of Mechanical Engineering, Tianjin University, 300350 Tianjin, China

^d Institut FEMTO-ST, CNRS, Univ. Bourgogne Franche-Comté, 25030 Besançon, France

ARTICLE INFO

Keywords:

Fluid-saturated porous media
Phononic crystals
Interface effects
Complex band structures

ABSTRACT

The propagation of waves in fluid-saturated porous periodic structures is significantly affected by the interface condition between adjacent layers. We consider in this paper the partial-open pore interface condition between adjacent layers in a one-dimensional fluid-saturated porous phononic crystal. A transfer matrix method is devised to obtain both the complex band structure and the poroelastic Bloch waves of the crystal. Spectral transmission through a finite structure is further computed by a stiffness matrix method. Attention is restricted to normal incidence of longitudinal waves. The influence of the pore blockage, a parameter of the partial-open pore interface condition, and of porosity and viscosity are investigated. The value of the pore blockage is found to influence significantly both the dispersion of poroelastic waves but also the partition of wave energy between solid skeleton and pore fluid. The effects of porosity and viscosity in the case of the partial-open pore interface condition are similar to what was previously obtained in the fully open pore case.

1. Introduction

Phononic crystals [1] (PCs) are artificial periodic composites that can control the propagation of acoustic/elastic waves. They can possess bandgaps [2,3] due to either Bragg scattering [1] or local resonance [4]. Strong dispersion may also be observed in the passing bands [5]. PCs can further exhibit peculiar properties, such as a negative effective mass density [6,7], waveguiding [8,9], negative refraction [10,11], or focusing [12,13].

In the frequent case that PCs are composed of different materials, there are interfaces between the latter. Those interfaces between the same or different material phases can be considered as perfect or imperfect. The influence of interface boundary conditions on wave propagation in PCs is a growing research direction [14]. Li et al. [15,16] computed the band structure and the transmission of elastic waves for two dimensional solid/solid smooth-contact interface PCs. Albuquerque and Sesion [17] studied acoustic wave propagation in solid/fluid superlattices. Xu et al. [18] calculated the band structure of two dimensional solid/air hierarchical PCs. Wang et al. [19] showed that the fluid/solid interface plays an important role in controlling elastic wave propagation by local additions of a fluid. Wee et al. [20] demonstrated the manipulation of surface guided modes at a solid/fluid interface. Zhen

et al. [21,22] examined the surface/interface effects on the propagation of transverse waves in two-dimensional nanoscale PCs.

The works mentioned above focused mostly on single-phased media. Recently, increasing attention has been paid to PCs composed of two- or multi-phased materials. Alevizaki et al. [23] extended the layer-multiple-scattering method to PCs of poroelastic spheres immersed in a fluid medium. Jiang and Huang [24] realized gradient sound absorbers with periodic macro void structure. Zhu et al. [25] put periodic metamaterial resonators in a porous layer to achieve broadband low-frequency sound absorption. Wang et al. [26,27] studied wave propagation in one-dimensional and two-dimensional fluid-saturated porous metamaterials (FSPM). Shi et al. [28–30] investigated the mitigation of vibrations in saturated soil with periodic pile barriers.

It is worth pointing out that the effect of different interface boundary conditions has mostly been considered for a single interface, but not for multi-phase PCs. The scattering of waves at the interface between different porous media has indeed been studied extensively. Geertsma and Smit [31] demonstrated that the slow longitudinal wave is generated at any interface between a porous medium and another medium. Lovera [32] derived general boundary conditions for interfaces with arbitrary shapes between porous media and other media. Rasolofoaon [33] showed that fluid transfer at the interface between a liquid and

* Corresponding author.

** Co-corresponding author.

E-mail addresses: ywang@tju.edu.cn (Y.-S. Wang), wangyanfeng@tju.edu.cn (Y.-F. Wang).

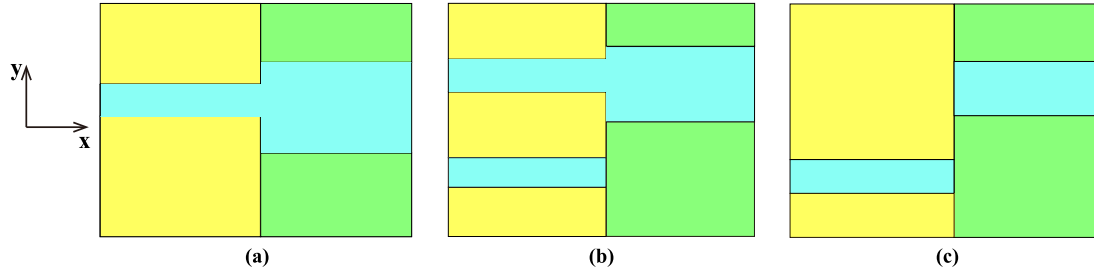


Fig. 1. Schematic representation of different interfaces between two FSP media, seen at the microscopic scale, adapted from Ref. [38]. (a) Open pore interface. (b) partial-open pore interface. (c) Sealed pore interface. The yellow and green areas represent the solid skeletons, and the blue areas represent fluid. (For interpretation of the references to color in this figure legend, the reader is referred to the web version of this article.)

a porous medium is important for the generation of the slow longitudinal wave. Wu et al. [34] and Denneman [35] investigated the reflection and the transmission of elastic waves between a porous medium and fluid. Vashisth et al. [36] studied elastic wave propagation through the dislocation-like interface between an elastic solid and a porous medium. The discussion was later extended to the reflection and the refraction of seismic waves between elastic and porous half-planes [37]. Following Deresiewicz and Skalak [38], Kumar and Miglani [39] discussed the effects of pore blockage on surface wave propagation across the interface between two dissimilar porous media. Sharma [40] investigated the influence of different sets of boundary conditions on the energy partition across the porous-porous interface.

In this paper, we focus on poroelastic wave propagation in one-dimensional fluid-saturated porous phononic crystals (FSPPC) with varying interface conditions parameterized by the pore blockage parameter. By using a transfer matrix method, complex band structures are obtained, as well as the eigenmodes at selected points. Transmission through finite structures is calculated by using a stiffness matrix method. The influence on wave propagation of the pore blockage and of the material parameters of the pore fluid is discussed. Only normal incidence is considered throughout the paper and attention is limited to the two longitudinal waves of fluid-saturated porous media.

2. Problem statement and mathematical formulation

2.1. Interface conditions between two FSP media

Following Deresiewicz [38], the interface boundary condition between two FSP materials can be simplified into one of the three models depicted in Fig. 1. The interface boundary condition in Fig. 1(a) is the open pore interface, for which the pores of the two FSP media are fully connected at the interface, so that the fluid can flow in between them. This is the case considered previously for FSP phononic crystals [26,27]. The interface boundary condition in Fig. 1(c) is called the sealed-pore interface. In this case there is no connection between the pores of both FSP materials and the fluid is sealed inside each of them. The interface boundary condition in Fig. 1(b) is the intermediate case where the pores of two FSP media are partially connected. It is also termed the partial-open pore interface. The average area at the interface where flow is possible is smaller than the intersection area of the pores on either side of the interface. Considering homogenized quantities, the flow through the interface produces a pressure drop or discontinuity, which is translated in the interface boundary condition [38]

$$p^{(1)} - p^{(2)} = h\dot{w}_n \quad (1)$$

where h is the pore blockage coefficient representing the effect of the area of the pore being blocked, with units Pa·s/m. \dot{w}_n is the relative particle velocity in the fluid measured in the normal direction.

2.2. Solution of wave equations

In this paper, we consider a one-dimensional FSP periodic structure composed of two materials A (yellow color) and B (grey color), as shown

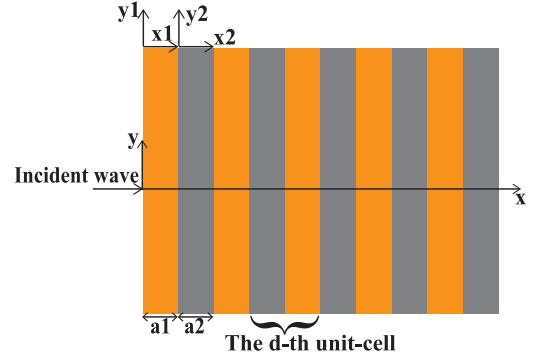


Fig. 2. Schematic representation of a 1D fluid-saturated porous phononic crystal. The lattice constant is $a = a_1 + a_2$. Periodicity is along the x direction; the other two directions are infinite. The alternating layers are considered as homogenized fluid-saturated porous media.

in Fig. 2. Both materials are isotropic. The geometrical and physical parameters of the present A-B system are the same as those considered in Ref. [26] and the basic equations in this section were mostly given therein. In the present work, we only consider normal incidence of waves. In this case, the shear wave is uncoupled from the two longitudinal waves and is disregarded in the analysis.

On the basis of Biot's theory [41], the constitutive equations for isotropic FSP media are expressed as

$$\begin{aligned} \sigma_{xx}^{(j)} &= (2B_1^{(j)} + B_2^{(j)})e_{xx}^{(j)} + B_3^{(j)}\xi^{(j)}, \\ p_x^{(j)} &= B_3^{(j)}e_{xx}^{(j)} + B_4^{(j)}\xi^{(j)}, \end{aligned} \quad (2)$$

where $j = 1, 2$ refers to the first and second layers of the unit-cell. $\sigma_{xx}^{(j)}$ and $e_{xx}^{(j)}$ are the stress and strain of the solid skeleton. $p_x^{(j)}$ is the pore pressure, and $\xi^{(j)}$ is the increment of the fluid content per unit volume. The displacement components of the skeleton and of the fluid are denoted as $u_x^{(j)}$ and $U_x^{(j)}$, respectively. The strain and the increment can be expressed as

$$e_{xx}^{(j)} = u_{x,x}^{(j)}, \quad \xi^{(j)} = w_{x,x}^{(j)}, \quad (3)$$

where $w_x^{(j)} = \phi^{(j)}(U_x^{(j)} - u_x^{(j)})$; and $\phi^{(j)}$ is the porosity of the materials. The material coefficients $B_1^{(j)}$ and $B_4^{(j)}$ are spatially periodic and determined by the materials properties of the solid skeleton and fluid [42]:

$$\begin{aligned} B_1^{(j)} &= C_{44}^{(j)}, \\ B_2^{(j)} &= C_{12}^{(j)} + B_3^{(j)}B_4^{(j)}/B_4^{(j)}, \\ B_3^{(j)} &= -\left(1 - \frac{C_{11}^{(j)} + 2C_{12}^{(j)}}{3K_s^{(j)}}\right)B_4^{(j)}, \\ B_4^{(j)} &= \left(\frac{1 - \phi^{(j)}}{K_s^{(j)}} + \frac{\phi^{(j)}}{K_f^{(j)}} - \frac{C_{11}^{(j)} + 2C_{12}^{(j)}}{3K_s^{(j)}K_s^{(j)}}\right)^{-1}, \end{aligned} \quad (4)$$

where $C_{11}^{(j)}$, $C_{12}^{(j)}$ and $C_{44}^{(j)}$ are the elastic constants of the solid skeleton. $K_s^{(j)}$ and $K_f^{(j)}$ represent the bulk modulus of the solid skeleton and of the pore fluid, respectively. The equations of motion can be expressed in local coordinates as

$$\begin{aligned} \sigma_{xx}^{(j)} &= \rho^{(j)} \ddot{u}_x^{(j)} + \rho_f^{(j)} \ddot{w}_x^{(j)}, \\ -p_{x,x}^{(j)} &= \rho_f^{(j)} \ddot{u}_x^{(j)} + m_{11}^{(j)} \ddot{w}_x^{(j)} + r_{11}^{(j)} \dot{w}_x^{(j)}, \end{aligned} \quad (5)$$

where $\rho^{(j)} = (1 - \phi^{(j)})\rho_s^{(j)} + \phi^{(j)}\rho_f^{(j)}$, $\rho_s^{(j)}$ and $\rho_f^{(j)}$ are the mass densities of the solid skeleton and of the pore fluid, respectively. $m_{11}^{(j)}$ and $r_{11}^{(j)}$ are coefficients introduced by Biot. For isotropic FSP materials, we have $m_{11}^{(j)} = m^{(j)}$ and $r_{11}^{(j)} = r^{(j)}$.

It is worth noting that Biot's theory conforms to the actual interpretation of elastic wave propagation when describing the macroscopic mechanical behavior of liquid-saturated porous media. However, it cannot fully reveal the actual phases within the porous medium and the interactions between those phases when the micro-mechanical behaviour is of interest. In this case, models containing different constituents and taking into account their physical boundaries are required [43].

Substituting Eq. (5) into Eq. (2), the wave equations of FSP media are obtained as

$$\begin{aligned} (2B_1^{(j)} + B_2^{(j)}) \frac{\partial^2 u_x^{(j)}}{(\partial x^{(j)})^2} - B_3^{(j)} \frac{\partial^2 w_x^{(j)}}{(\partial x^{(j)})^2} &= \rho^{(j)} \ddot{u}_x^{(j)} + \rho_f^{(j)} \ddot{w}_x^{(j)}, \\ -B_3^{(j)} \frac{\partial^2 u_x^{(j)}}{(\partial x^{(j)})^2} + B_4^{(j)} \frac{\partial^2 w_x^{(j)}}{(\partial x^{(j)})^2} &= \rho_f^{(j)} \ddot{u}_x^{(j)} + m^{(j)} \ddot{w}_x^{(j)} + r^{(j)} \dot{w}_x^{(j)}, \end{aligned} \quad (6)$$

For time-harmonic plane waves, we have

$$\begin{aligned} u_x^{(j)} &= A^{(j)} \exp(iq^{(j)}x^{(j)}) \exp(-i\omega t), \\ w_x^{(j)} &= C^{(j)} \exp(iq^{(j)}x^{(j)}) \exp(-i\omega t), \end{aligned} \quad (7)$$

where $i = \sqrt{-1}$, $x^{(j)} \in (0, a_j)$ and a_j is the thickness of the j -th layer of the unit cell. The lattice constant is $a = a_1 + a_2$. $q^{(j)}$ is the wavenumber along the x direction. $[A^{(j)}, C^{(j)}]$ are coefficients to be determined. Substitution of Eq. (7) into Eq. (6) leads to the following equations:

$$\begin{aligned} (\rho^{(j)}\omega^2 - (2B_1^{(j)} + B_2^{(j)})(q^{(j)})^2)A^{(j)} \\ + (B_3^{(j)}(q^{(j)})^2 + \rho_f^{(j)}\omega^2)C^{(j)} &= 0, \\ (B_3^{(j)}(q^{(j)})^2 + \rho_f^{(j)}\omega^2)A^{(j)} \\ + (\bar{m}^{(j)}\omega^2 - B_4^{(j)}(q^{(j)})^2)C^{(j)} &= 0, \end{aligned} \quad (8)$$

where $\bar{m}^{(j)} = m^{(j)} + \frac{i\gamma^{(j)}}{\omega}$. The existence of non-trivial solutions of Eq. (8) requires that the determinant of the coefficient matrix is zero. Therefore, we have

$$\begin{vmatrix} \rho^{(j)}\omega^2 - (2B_1^{(j)} + B_2^{(j)})(q^{(j)})^2 & B_3^{(j)}(q^{(j)})^2 + \rho_f^{(j)}\omega^2 \\ B_3^{(j)}(q^{(j)})^2 + \rho_f^{(j)}\omega^2 & \bar{m}^{(j)}\omega^2 - B_4^{(j)}(q^{(j)})^2 \end{vmatrix} = 0. \quad (9)$$

Eq. (9) admits two solutions for $(q^{(j)})^2$. Hence, there are two pairs of roots they are opposite to each other

$$\begin{aligned} q_1^{(j)} = -q_2^{(j)} &= \omega \sqrt{\frac{-G_2^{(j)} + \sqrt{G_2^{(j)}G_2^{(j)} - 4G_1^{(j)}G_3^{(j)}}}{2G_1^{(j)}}}, \\ q_3^{(j)} = -q_4^{(j)} &= \omega \sqrt{\frac{-G_2^{(j)} - \sqrt{G_2^{(j)}G_2^{(j)} - 4G_1^{(j)}G_3^{(j)}}}{2G_1^{(j)}}}, \end{aligned} \quad (10)$$

with $G_1^{(j)} = (2B_1^{(j)} + B_2^{(j)})B_4^{(j)} - B_3^{(j)}B_3^{(j)}$, $G_2^{(j)} = \rho^{(j)}\bar{m}^{(j)} - \rho_f^{(j)}\rho_f^{(j)}$ and $G_3^{(j)} = -(2B_1^{(j)} + B_2^{(j)})\bar{m}^{(j)} - \rho_f^{(j)}B_4^{(j)} - 2\rho_f^{(j)}B_3^{(j)}$. The positive (negative)

value of a root means that the wave propagates in the positive (negative) direction along the x direction. $q_1^{(j)}$ and $q_3^{(j)}$ represent the coupled slow (P2) and fast (P1) longitudinal wave, respectively. For each $q_l^{(j)}$ ($l = 1 \sim 4$), the amplitude ratios of the waves can be expressed according to Eq. (8) as

$$f_l^{(j)} = \frac{C_l^{(j)}}{A_l^{(j)}} = \frac{(2B_1^{(j)} + B_2^{(j)})(q_l^{(j)})^2 - \rho_f^{(j)}\omega^2}{B_3^{(j)}(q_l^{(j)})^2 + \rho_f^{(j)}\omega^2}. \quad (11)$$

The displacement of the fundamental wave decomposes into slow and fast longitudinal waves. According to Eqs. (7), (10) and (11), the general solution for the displacement can be written as

$$\begin{aligned} u_x^{(j)} &= \sum_{l=1}^4 A_l^{(j)} \exp(iq_l^{(j)}x^{(j)}) \exp(-i\omega t), \\ w_x^{(j)} &= \sum_{l=1}^4 f_l^{(j)} A_l^{(j)} \exp(iq_l^{(j)}x^{(j)}) \exp(-i\omega t). \end{aligned} \quad (12)$$

Substituting Eq. (12) into Eq. (2), the stress and pressure general solution are obtained as

$$\begin{aligned} \sigma_{xx}^{(j)} &= \sum_{l=1}^4 n_l^{(j)} A_l^{(j)} \exp(iq_l^{(j)}x^{(j)}) \exp(-i\omega t), \\ p_x^{(j)} &= \sum_{l=1}^4 g_l^{(j)} A_l^{(j)} \exp(iq_l^{(j)}x^{(j)}) \exp(-i\omega t), \end{aligned} \quad (13)$$

where $g_l^{(j)} = iq_l^{(j)}[(2B_1^{(j)} + B_2^{(j)}) - B_3^{(j)}f_l^{(j)}]$, $n_l^{(j)} = iq_l^{(j)}(B_3^{(j)} - B_4^{(j)}f_l^{(j)})$.

2.3. Transfer matrix

We now consider the propagation of elastic waves in the isotropic FSP periodic structure with partial-open pore interfaces. To calculate the transfer matrix, we define the state vector as $\mathbf{V} = [u_x, w_x, \sigma_{xx}, p_x]^T$. For the d th unit-cell, the state vectors at the left and right sides of the j th layer can be written as

$$\begin{aligned} [\mathbf{V}_L^{(j)}]^{(d)} &= [u_x^{(j)}, w_x^{(j)}, \sigma_{xx}^{(j)}, p_x^{(j)}]_{x^{(j)}=0}^T \\ &= \mathbf{P}_L^{(j)} [A_1^{(j)}, A_2^{(j)}, A_3^{(j)}, A_4^{(j)}]^T \exp(-i\omega t), \\ [\mathbf{V}_R^{(j)}]^{(d)} &= [u_x^{(j)}, w_x^{(j)}, \sigma_{xx}^{(j)}, p_x^{(j)}]_{x^{(j)}=a_j}^T \\ &= \mathbf{P}_R^{(j)} [A_1^{(j)}, A_2^{(j)}, A_3^{(j)}, A_4^{(j)}]^T \exp(-i\omega t). \end{aligned} \quad (14)$$

Here $\mathbf{P}_L^{(j)}$ and $\mathbf{P}_R^{(j)}$ are 4×4 matrices whose elements are listed in Appendix A.

For the interface between two layers of the d th unit cell, we obtain the following relationship using continuity conditions:

$$\begin{bmatrix} u_x^1 \\ w_x^1 \\ \sigma_{xx}^1 \\ p_x^1 \end{bmatrix}_{x^{(1)}=a_1}^{(d)} = \begin{bmatrix} u_x^2 \\ w_x^2 \\ \sigma_{xx}^2 + h w_x^2 \\ p_x^2 \end{bmatrix}_{x^{(2)}=0}^{(d)}. \quad (15)$$

Similarly, the continuity conditions at the interface between the $(d-1)$ th and the d th unit-cells can be expressed as

$$\begin{bmatrix} u_x^1 \\ w_x^1 \\ \sigma_{xx}^1 \\ p_x^1 \end{bmatrix}_{x^{(1)}=0}^{(d)} = \begin{bmatrix} u_x^2 \\ w_x^2 \\ \sigma_{xx}^2 \\ p_x^2 - h w_x^2 \end{bmatrix}_{x^{(2)}=a_2}^{(d-1)}. \quad (16)$$

Substituting Eq. (14) into Eqs. (15) and (16), we derive the following relation:

$$\begin{aligned} \mathbf{P}_R^1 \Psi_d^1 &= (\mathbf{P}_L^2 - i\omega h \mathbf{Y}) \Psi_d^2, \\ \mathbf{P}_L^1 \Psi_d^1 &= (\mathbf{P}_R^2 + i\omega h \mathbf{Z}) \Psi_{d-1}^2, \end{aligned} \quad (17)$$

where Ψ_{d-1}^j and Ψ_d^j are the amplitude vectors for the j th layer of the $(d-1)$ th and d th unit-cells. From Eq. (17), we have the following relation:

$$\Psi_d^2 = (\mathbf{P}_L^2 - i\omega h \mathbf{Y})^{-1} \mathbf{P}_R^1 (\mathbf{P}_L^1)^{-1} (\mathbf{P}_R^2 + i\omega h \mathbf{Z}) \Psi_{d-1}^2. \quad (18)$$

As a result, the transfer matrix of the adjacent cell can be expressed as

$$\mathbf{T}_d = (\mathbf{P}_L^2 - i\omega h \mathbf{Y})^{-1} \mathbf{P}_R^1 (\mathbf{P}_L^1)^{-1} (\mathbf{P}_R^2 + i\omega h \mathbf{Z}), \quad (19)$$

where \mathbf{Y} and \mathbf{Z} are 4×4 matrices whose elements are listed in Appendix A. For periodic structures, \mathbf{T}_d ($d = 1, 2, \dots, s$) are the same and are simply denoted \mathbf{T} . Because of periodicity along the x direction, Bloch's theorem implies

$$\Psi_d^2 = \exp(ik_x a) \Psi_{d-1}^2. \quad (20)$$

Substituting Eq. (20) into Eq. (18), we get

$$(\mathbf{T} - \exp(ik_x a) \mathbf{I}) \Psi_d^2 = 0. \quad (21)$$

Finally, we obtain the following eigenvalue equation:

$$|\mathbf{T} - \exp(ik_x a) \mathbf{I}| = 0, \quad (22)$$

where k_x is the Bloch wavenumber in the x direction and \mathbf{I} is the 4×4 identity matrix. For a given frequency, k_x can be obtained by solving Eq. (21). As a result, the complex band structure $k_x(\omega)$ can be obtained.

2.4. Modal distribution

Combining Eqs. (17) and (21), we have

$$\begin{aligned} (\mathbf{T} - \exp(ik_x a) \mathbf{I}) (\mathbf{P}_R^2 + i\omega h \mathbf{Z})^{-1} \mathbf{P}_L^1 [A_1^1, A_2^1, A_3^1, A_4^1]^T \exp(-i\omega t) &= 0, \\ [A_1^2, A_2^2, A_3^2, A_4^2]^T - (\mathbf{P}_L^2 - i\omega h \mathbf{Y})^{-1} \mathbf{P}_R^1 [A_1^1, A_2^1, A_3^1, A_4^1]^T &= 0. \end{aligned} \quad (23)$$

Solving Eq. (22), we obtain the amplitude ratio relations:

$$\begin{aligned} A_2^1 &= Q_1 A_1^1, A_3^1 = R_1 A_1^1, A_4^1 = S_1 A_1^1, \\ A_1^2 &= O_2 A_1^1, A_2^2 = Q_2 A_1^1, A_3^2 = R_2 A_1^1, A_4^2 = S_2 A_1^1. \end{aligned} \quad (24)$$

The expressions of the proportionality coefficients are listed in Appendix B.

Substituting Eq. (22) into Eq. (12), the displacement can be written as

$$\begin{aligned} u_{x1} &= (\exp(iq_1^1 x) + Q_1 \exp(iq_2^1 x)) A_1^1 \exp(-i\omega t) \\ &\quad + (R_1 \exp(iq_3^1 x) + S_1 \exp(iq_4^1 x)) A_1^1 \exp(-i\omega t), \\ w_{x1} &= (f_1^1 \exp(iq_1^1 x) + f_2^1 Q_1 \exp(iq_2^1 x)) A_1^1 \exp(-i\omega t) \\ &\quad + (f_3^1 R_1 \exp(iq_3^1 x) + f_4^1 S_1 \exp(iq_4^1 x)) A_1^1 \exp(-i\omega t), x \in [0, a_1] \end{aligned} \quad (25)$$

and

$$\begin{aligned} u_{x2} &= (O_2 \exp(iq_1^2 x) + Q_2 \exp(iq_2^2 x)) A_1^1 \exp(-i\omega t) \\ &\quad + (R_2 \exp(iq_3^2 x) + S_2 \exp(iq_4^2 x)) A_1^1 \exp(-i\omega t), \\ w_{x2} &= (f_1^2 O_2 \exp(iq_1^2 x) + f_2^2 Q_2 \exp(iq_2^2 x)) A_1^1 \exp(-i\omega t) \\ &\quad + (f_3^2 R_2 \exp(iq_3^2 x) + f_4^2 S_2 \exp(iq_4^2 x)) A_1^1 \exp(-i\omega t), x \in [0, a_2]. \end{aligned} \quad (26)$$

The stresses and the pressure can be easily calculated in the same way.

2.5. Stiffness matrix method

The transfer matrix method may become unstable when the number of layers is large [44]. Some researchers have proposed stable solution methods, such as the stiffness matrix method [45]. In case our considerations were generalized to oblique incidence or to surface waves, it may be worthwhile considering scattering-matrix methods [46,47]. In this work, the stiffness matrix method is employed to calculate transmission spectra. In practice, the stiffness matrix reflects the relationship between displacements and stresses. Similarly to Ref. [48], we also assume that the generalized displacements and stresses are $[\sigma_1, \mathbf{u}_1]^T$ at the left boundary of the first layer, $[\sigma_2, \mathbf{u}_2]^T$ at the interface between the two sub-layers, and $[\sigma_3, \mathbf{u}_3]^T$ at the right boundary of the second layer. According to the constitutive relation [45], we have the following relationship:

$$\begin{aligned} \begin{bmatrix} \sigma_1 \\ \sigma_2 \end{bmatrix} &= \begin{bmatrix} \mathbf{K}_{11}^A & \mathbf{K}_{12}^A \\ \mathbf{K}_{21}^A & \mathbf{K}_{22}^A \end{bmatrix} \begin{bmatrix} \mathbf{u}_1 \\ \mathbf{u}_2 \end{bmatrix}, \\ \begin{bmatrix} \sigma_2 \\ \sigma_3 \end{bmatrix} &= \begin{bmatrix} \mathbf{K}_{11}^B & \mathbf{K}_{12}^B \\ \mathbf{K}_{21}^B & \mathbf{K}_{22}^B \end{bmatrix} \begin{bmatrix} \mathbf{u}_2 \\ \mathbf{u}_3 \end{bmatrix}, \end{aligned} \quad (27)$$

where \mathbf{K}^A and \mathbf{K}^B is 4×4 stiffness matrices of the first and the second layer. Their expressions are

$$\begin{aligned} \mathbf{K}^A &= \mathbf{E}_\sigma^1 (\mathbf{E}_u^1)^{-1}, \\ \mathbf{K}^B &= \mathbf{E}_\sigma^2 (\mathbf{E}_u^2)^{-1}. \end{aligned} \quad (28)$$

We can easily write the local stiffness matrix of the unit cell by eliminating σ_2 and \mathbf{u}_2 of Eq. (27):

$$\begin{aligned} \begin{bmatrix} \sigma_1 \\ \sigma_3 \end{bmatrix} &= \bar{\mathbf{K}} \begin{bmatrix} \mathbf{u}_1 \\ \mathbf{u}_3 \end{bmatrix}, \\ \bar{\mathbf{K}} &= \begin{bmatrix} \mathbf{K}_{11}^A + \mathbf{K}_{12}^A (\mathbf{K}_{11}^B - \mathbf{K}_{22}^A)^{-1} \mathbf{K}_{21}^A & -\mathbf{K}_{12}^A (\mathbf{K}_{11}^B - \mathbf{K}_{22}^A)^{-1} \mathbf{K}_{12}^B \\ \mathbf{K}_{21}^B (\mathbf{K}_{11}^B - \mathbf{K}_{22}^A)^{-1} \mathbf{K}_{21}^A & \mathbf{K}_{22}^B - \mathbf{K}_{12}^B (\mathbf{K}_{11}^B - \mathbf{K}_{22}^A)^{-1} \mathbf{K}_{21}^B \end{bmatrix}. \end{aligned} \quad (29)$$

When the periodic structure is composed of b unit cells, the \mathbf{K}^A and \mathbf{K}^B matrices can be treated as the global stiffness matrix \mathbf{K}^{b-1} for the left $(b-1)$ unit cells and the local stiffness matrix \mathbf{K}^b of the b th unit cell. In addition, the stiffness matrix expression of the whole structure can be written

$$\begin{aligned} \mathbf{K} &= \begin{bmatrix} \mathbf{K}_{11} & \mathbf{K}_{12} \\ \mathbf{K}_{21} & \mathbf{K}_{22} \end{bmatrix}, \\ \mathbf{K}_{11} &= \mathbf{K}_{11}^{b-1} + \mathbf{K}_{12}^{b-1} (\mathbf{K}_{11}^b - \mathbf{K}_{22}^{b-1})^{-1} \mathbf{K}_{21}^{b-1}, \\ \mathbf{K}_{12} &= -\mathbf{K}_{12}^{b-1} (\mathbf{K}_{11}^b - \mathbf{K}_{22}^{b-1})^{-1} \mathbf{K}_{12}^b, \\ \mathbf{K}_{21} &= \mathbf{K}_{21}^b (\mathbf{K}_{11}^b - \mathbf{K}_{22}^{b-1})^{-1} \mathbf{K}_{21}^{b-1}, \\ \mathbf{K}_{22} &= \mathbf{K}_{22}^b - \mathbf{K}_{12}^b (\mathbf{K}_{11}^b - \mathbf{K}_{22}^{b-1})^{-1} \mathbf{K}_{21}^b. \end{aligned} \quad (30)$$

It should be stressed that the above derivation assumes that the generalized displacements and stresses are continuous at the interface. However, there is a pressure drop at the interface for the partial-open pore interface. Therefore, we should write down the equivalent pressure to keep continuous generalized stresses at the interface. Substituting Eq. (1) into Eq. (28), we can calculate the local stiffness matrix of the unit-cell.

For the first unit cell, we need to write the equivalent pressure at the interface between two sub-layers. The elements of matrices $\mathbf{E}_{u_1}^1$, $\mathbf{E}_{\sigma_1}^1$, $\mathbf{E}_{u_2}^1$ and $\mathbf{E}_{\sigma_2}^1$ are listed in Appendix C. For the remaining unit cells, the pressure is continuous not only at the interface of the two sub-layers, but also at the interface of the adjacent cells. The elements of the matrix $\mathbf{E}_{\sigma_1}^2$ are given in Appendix C. The other matrices obey the following relations: $\mathbf{E}_{u_1}^2 = \mathbf{E}_{u_1}^1$, $\mathbf{E}_{\sigma_2}^2 = \mathbf{E}_{\sigma_2}^1$, and $\mathbf{E}_{\sigma_2}^2 = \mathbf{E}_{\sigma_2}^1$.

We assume that the periodic structure is placed between two semi-infinite homogeneous media. The P_2 wave is incident from the left. As a result, the displacements of the incident wave field can be written as

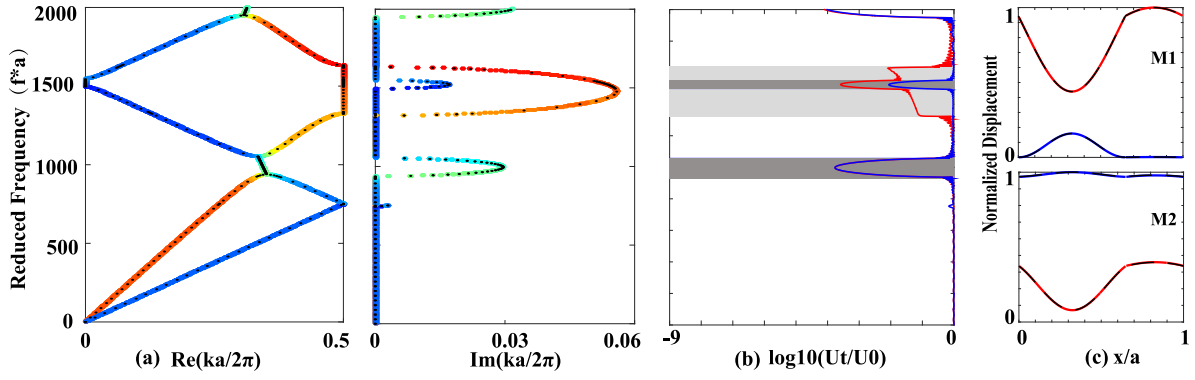


Fig. 3. Complex band structure for one-dimensional FSPPC with the open-pore interface. Panel (a) consists of two parts: the left and right parts show the relation of reduced frequency with the real and imaginary parts of the wave number, respectively. The black dots represent the complex band structure calculated by FEM. The color scale from blue to red represents the relative energy ratio from 0 to 1. The transmission curves for 50-unit cells structure are plotted in panel (b). The red (blue) line represents the displacement transmission coefficient T_{P1}/U_0 (T_{P2}/U_0) under the incidence of the P1 (P2) wave. The gray regions represent the complete band gaps for both P1 and P2 waves in panel (a), while the light gray region shows the Bragg band gap for P1 wave. Panel (c) shows the normalized displacement distribution red u_x for and blue for w_x at the marked points in panel (a) at 429 m/s. The relative energy ratio is 0.7719 at point M1 and 0.2436 at point M2. The black dashed lines are the results obtained by FEM. (For interpretation of the references to color in this figure legend, the reader is referred to the web version of this article.)

$$\begin{aligned} u_{x0} &= \exp(iq_1^1 x_0)U_0 + \exp(iq_2^1 x_0)R_{P2} + \exp(iq_4^1 x_0)R_{P1}, \\ w_{x0} &= f_1^1 \exp(iq_1^0 x_0)U_0 + f_2^1 \exp(iq_2^0 x_0)R_{P2} + f_4^1 \exp(iq_4^0 x_0)R_{P1}, \end{aligned} \quad (31)$$

where U_0 is the amplitude of the incident waves. R_{P2} and R_{P1} are the amplitudes of the reflected waves. The subscript 0 represents the left infinite structure. Similarly, we can write the transmitted displacement as

$$\begin{aligned} u_{xs} &= \exp(iq_1^2 x_s)T_{P2} + \exp(iq_3^2 x_s)T_{P1}, \\ w_{xs} &= f_1^2 \exp(iq_1^2 x_s)T_{P2} + f_3^2 \exp(iq_3^2 x_s)T_{P1}, \end{aligned} \quad (32)$$

where T_{P2} and T_{P1} are the transmitted amplitudes and the subscript s represents the right infinite structure. Therefore, the relation between displacements and stresses at the boundaries can be expressed by using the stiffness matrix as

$$\begin{bmatrix} \sigma_0 \\ \sigma_s \end{bmatrix} = \mathbf{K} \begin{bmatrix} \mathbf{u}_0 \\ \mathbf{u}_s \end{bmatrix}, \quad (33)$$

where $\sigma_0 = [\sigma_{x0}, p_{x0}]^T$ and $\mathbf{u}_0 = [u_{x0}, w_{x0}]^T$ are the stresses and the displacements of the incident wave. $\sigma_s = [\sigma_{xs}, p_{xs}]^T$ and $\mathbf{u}_s = [u_{xs}, w_{xs}]^T$ are the transmitted stresses and displacements. Substituting Eqs. (30) and (31) into Eq. (32), we obtain the transmission and reflection coefficients:

$$\begin{bmatrix} \frac{R_{P2}}{U_0} & \frac{R_{P1}}{U_0} & \frac{T_{P2}}{U_0} & \frac{T_{P1}}{U_0} \end{bmatrix} = \mathbf{M}^{-1} \mathbf{N}_{P2}, \quad (34)$$

where R_{P2}/U_0 and R_{P1}/U_0 are reflection displacement coefficients. T_{P2}/U_0 and T_{P1}/U_0 are transmitted displacement coefficients. The elements of matrices \mathbf{M} and \mathbf{N}_{P2} are listed in Appendix D. When the incident wave is the P1 wave, \mathbf{N}_{P2} must be replaced by \mathbf{N}_{P1} . The elements of \mathbf{N}_{P1} are also listed in Appendix D.

3. Numerical results and discussion

In this section, we consider Bloch wave propagation in 1D FSP phononic crystal with partial-open pore interfaces. Complex band structures, transmission spectra, as well as eigenmodes are calculated by using the theory in section 2 for the same material parameters as in Ref. [26]. The ratio of the thicknesses of the two materials (saturated soil and concrete) is arbitrarily chosen as 13 : 7, for definiteness. We have checked that the conclusions are not significantly affected if this ratio is modified. For comparison with previous finite element results [26], the open pore case is considered first, before moving to the partial-open pore case. The influence of porosity is considered last.

3.1. Open pore interface

First, we consider the case of open pore interface by setting $h = 0$ Pa.s/m. There is no pressure difference at the interface, so the displacement, the stress and the pressure are all continuous at the interface. As a note, we choose $\alpha_j(\infty) = 1.02$ throughout this paper. The complex band structure is shown in Fig. 3(a). The black dots represent the results obtained by the finite element method (FEM). They are fully consistent with the transfer matrix method. The color scale represents the relative energy ratio of the kinetic-energy in the solid skeleton to the total kinetic energy:

$$P_s = \frac{\int e^s dx}{(\int e^s + e^f) dx}, \quad (35)$$

where $e^s = (1 - \phi)\rho_s \omega^2 u_x^2 / 2$ and $e^f = \phi \rho_f \omega^2 U_x^2 / 2$ represent the kinetic energy densities for the solid skeleton and the pore fluid, respectively. The line integration is along the unit cell. The consideration of the relative energy ratio allows us to identify the relation of each band with the fast longitudinal wave (P1 wave) and the slow longitudinal wave (P2 wave). The first two bands are of almost pure relative energy ratio but undergo an anti-crossing around a reduced frequency of 1000 m/s [26]. Note that the relative energy ratio of Bloch waves is generally mixed with P1 and P2 components. In the following, bands whose color is close to red are termed quasi-P1 (QP1), whereas bands whose color is close to blue are termed quasi-P2 (QP2).

In addition, the transmission spectra of a finite structure with 50 unit cells are calculated by using the stiffness matrix method and are shown in Fig. 3(b). The red (blue) line represents the displacement transmission coefficient T_{P1}/U_0 (T_{P2}/U_0) under the incidence of a source P1 (P2) wave. The eigenmodes at the selected points M1 and M2 just below the anti-crossing of the P1 and the P2 waves are plotted in Fig. 3(c) and are obtained according to Eqs. (25)–(26). For comparison, the eigenmodes calculated by FEM are also plotted in Fig. 3(c) with black dash lines. They match almost exactly with the transfer matrix results. As a note, the transfer matrix method is faster than 1D FEM and is in principle much more precise, since its derivation does not rely on any approximation. Its main disadvantage is that it is specialized to one-dimensional structures.

3.2. Partial-open pore interface

In this section, we focus on wave propagation in 1D FSP phononic crystal with partial-open pore interfaces by varying the pore blockage

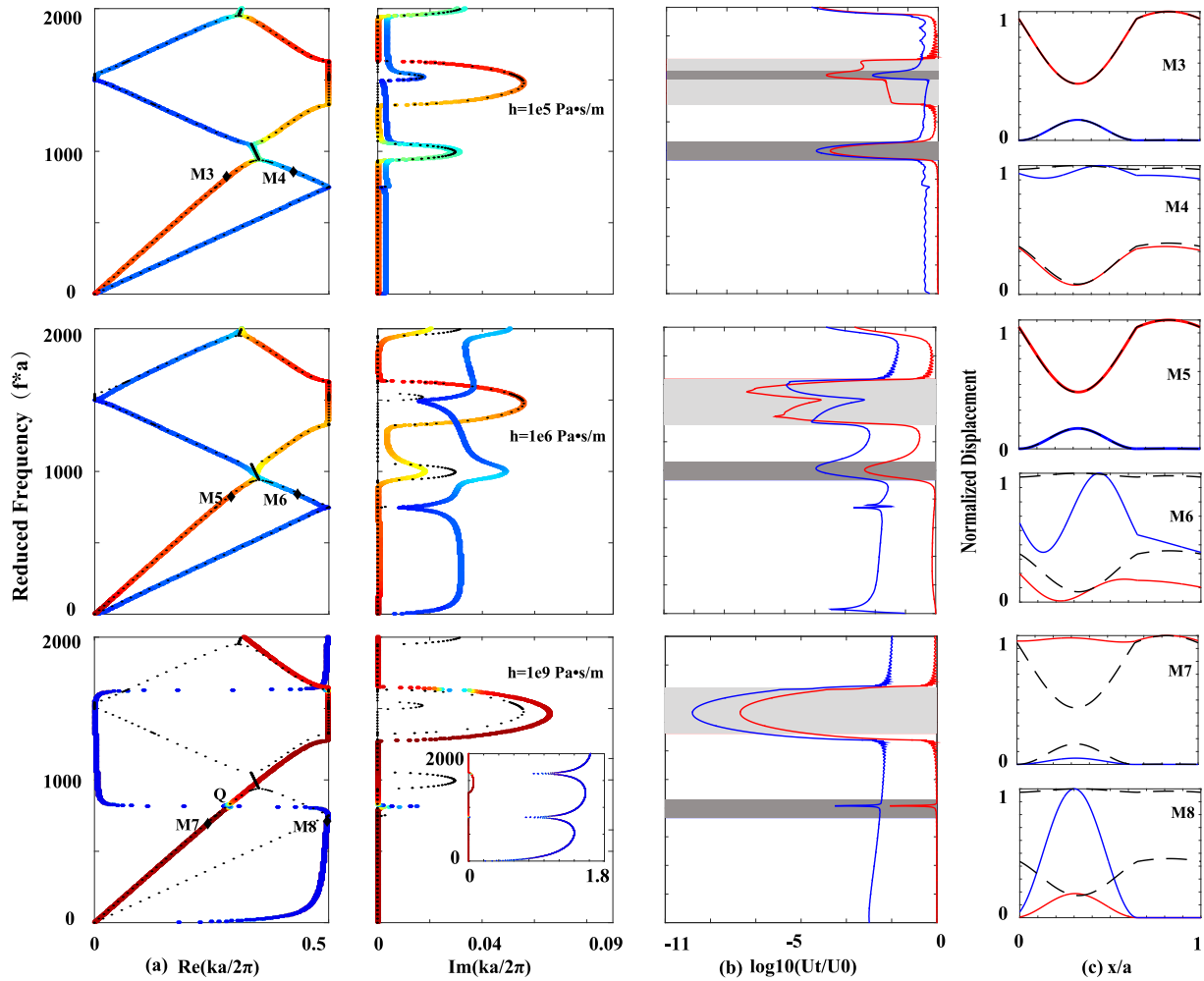


Fig. 4. Complex band structure for the 1D FSPPC with the partial-open pore interface. The left and right parts in panel (a) stand for the relation of the reduced frequency with the real and imaginary parts of the wave number, respectively. The color scale is the same as that in Fig. 3. The black dots represent the complex band structure calculated by FEM. The inset represents a larger view of the imaginary part of the wave number. The calculated transmissions of a finite structure with 50 unit cells are plotted in panel (b). The red (blue) line represents the displacement transmission coefficient T_{P1}/U_0 (T_{P2}/U_0) under the incidence of the P1 (P2) wave. Panel (c) shows the normalized displacement distribution at the marked points in panel (a). The relative energy ratio at marked points is 0.7719 (M3), 0.2416 (M4), 0.7725 (M5), 0.2106 (M6), 0.986 (M7) and 0.0957 (M8). (For interpretation of the references to color in this figure legend, the reader is referred to the web version of this article.)

coefficient h . In this case, the displacement and stress at the interface remain continuous, but the pressure is discontinuous according to Eq. (1). The numerical results are summarized in Fig. 4.

When the value of the pore blockage coefficient is rather small ($h = 10^5$ Pa*s/m), the main change compared to the open pore condition is the appearance of a small imaginary part of the Bloch wavenumber, even at low frequencies. The real part of the complex band structure concurrently shows very limited changes. The degenerated evanescent bands in the avoided-crossing start to separate gradually. The imaginary part of the QP2 wave increases slightly at all frequencies and thus turns into an evanescent wave. This change reflects in the decrease of the transmission coefficient T_{P2}/U_0 under P2 wave incidence, whereas T_{P1}/U_0 is almost unchanged. Looking at the relative energy ratio just below the anti-crossing, the modal distribution at point M3 (M4, respectively) is almost identical to that at point M1 (M2, resp.) for the open pore case.

Increasing the pore blockage coefficient ($h = 10^6$ Pa*s/m), the real band structure is further stretched around the anti-crossing as a system of two complex bands is forming, separating more neatly the QP1 and the QP2 waves. The imaginary part of the Bloch wavenumber for the QP2 wave increases notably. The Bragg gaps for the QP2 wave almost disappear, leaving only a reduced damping at the lower folding points on

the first Brillouin zone boundary. The QP1 wave acquires an imaginary component of the Bloch wavenumber around the frequencies of the anti-crossing, owing to the coupling between the QP1 and QP2 waves in this range. The transmission T_{P2}/U_0 for the QP2 wave is strongly reduced at all frequencies. Meanwhile, the transmission coefficient T_{P1}/U_0 for the QP1 wave is strengthened inside the first Bragg band gap but is not significantly changed otherwise. Looking at the relative energy ratio just below the anti-crossing, the modal distribution at point M5 is again almost identical to that at point M1 for the open pore case, but the modal distribution at point M6 differs from that at point M2 along the unit cell.

When the pore blockage coefficient is further increased ($h = 10^9$ Pa*s/m), the real part of the dispersion relation for the QP2 wave locates mostly around the high symmetry points of the Brillouin zone. Its imaginary part is actually very large at all frequencies. Meanwhile, the imaginary part of the dispersion of the QP1 wave is not affected, except inside the first Bragg gap where the attenuation is enhanced. As whole, the QP1 and QP2 waves become almost completely decoupled. Looking at the relative energy ratio just below the anti-crossing, the modal distribution at point M7 (QP1 branch) is almost purely in the solid skeleton, whereas the modal distribution at point M8 (QP2 branch) is dominantly in the pore fluid and is strongly attenuated by the partial-open pore interface boundary condition.

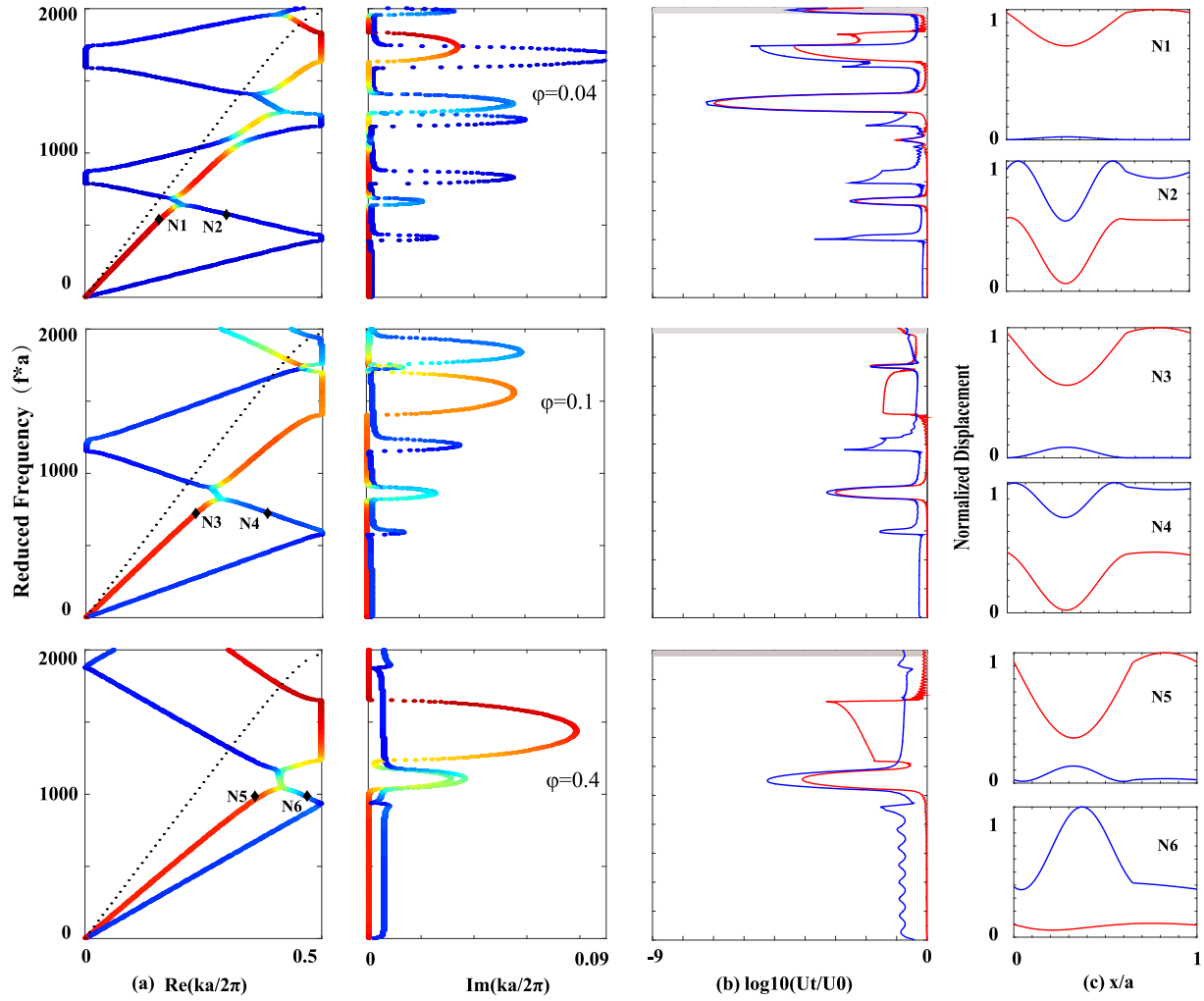


Fig. 5. Influence of the porosity parameter ϕ on the complex band structure for the 1D FSPPC with the partial-open pore interface ($h = 10^5$ Pa.s/m). Panel (a) shows the reduced frequency as a function of the real and of the imaginary parts of the reduced wavenumber. The color scale is the same as that in Fig. 3. Transmission spectra are plotted in panel (b). The red (blue) line represents the displacement transmission coefficient T_{p1}/U_0 (T_{p2}/U_0) under the incidence of the P1 (P2) wave. The relative energy ratio at marked points is 0.8824 (N1), 0.0984 (N2), 0.8147 (N3), 0.1827 (N4), 0.800 (N5) and 0.2126 (N6). (For interpretation of the references to color in this figure legend, the reader is referred to the web version of this article.)

Before ending this section, we would like to mention that since there is no connection between two porous media for the sealed pore interface, it is equivalently modeled by adding an impermeable membrane at the interface. This could be implemented by setting both $h = \infty$ and $\dot{w}_n = 0$ in Eq. (1). In this case, however, the pressure would not be specified and the pressure drop would remain uncertain. The complex band structure hence can not be solved for. Anyway, we can anticipate the infinite limit by removing the QP2 wave in the complex band structure and keeping only the QP1 bands. In the limit, the FSP phononic crystal behaves as an elastic phononic crystal for the QP1 wave only and a periodic lossy structure for the QP2 wave.

3.3. Influence of porosity

In this section, we focus on the influence of porosity on wave propagation through the FSP PCs with partial-open pore interfaces, for $h = 10^5$ Pa.s/m. The complex band structures and the transmission spectra are shown in Fig. 5 for selected values of the porosity. For comparison purposes, the band structure of the single-phase elastic PC is also plotted with dotted lines ($\phi = 0$), for which case there is only one longitudinal wave. When a small porosity ($\phi = 0.04$) is introduced, the phase velocity of the QP1 wave decreases. The QP2 wave branches cross four times the

QP1 wave branches in the considered frequency range, inducing four avoided crossings.

When the porosity increases, the phase velocity of the QP2 wave increases. Concurrently, the phase velocity of the QP1 wave decreases, but only slightly. As a result of the change in the slope of the branches, the number of avoided-crossings decreases. There are only two of them when $\phi = 0.1$ and only one when $\phi = 0.4$.

For the first anti-crossing, the frequency at which the QP1 and QP2 should intercept is given by the following relation [2]:

$$k_{p1}(\omega) = 2\pi/a - k_{p2}(\omega). \quad (36)$$

The following avoided-crossings are obtained by equating similar combinations of $\pm k_{p1}$ and $\pm k_{p1=2}$ with exactly a reciprocal lattice spacing. k_{p1} and k_{p2} are the wavenumbers of the P1 and P2 phonons, respectively, when they are unfolded into the extended Brillouin zone. As such, Eq. (36) describes a phonon-phonon scattering similar to an Umklapp scattering. It is worth noting that the second band gap is a bit complex, like a ‘wavenumber’ bandgap. In the pass band of QP2 wave, the imaginary wave number increases monotonically with porosity, leading to an overall small transmission (T_{p2}/U_0). It is also observed that the attenuation in the lowest avoided-crossing is more pronounced, as well as the

Bragg gap for the QP1 wave. These gaps also get wider with an increase in porosity, as verified with the transmission curves (Fig. 5(c)).

Furthermore, we have also considered the influence of the fluid viscosity on wave propagation in the FSPCs with partial-open pore interfaces. The results are similar to those for open pore interfaces [26] and are gathered in Appendix E.

4. Conclusions

In this paper, we have investigated wave propagation in 1D fluid-saturated porous phononic crystals with partial-open pore interfaces. Complex band structures and modal distributions were calculated by a transfer matrix method. Transmission spectra were calculated by a stiffness matrix method. Both transmission and transfer matrix methods were devised specifically for fluid-saturated porous media. The results for the open-pore interface agree exactly with previous finite element results [26]. The pore blockage coefficient, the fluid viscosity and the porosity all strongly influence wave propagation, and especially the existence of avoided-crossings between the fast and the slow longitudinal waves of fluid-saturated porous media. The value of the pore blockage is found to influence significantly both the dispersion of poroelastic waves but also the partition of wave energy between solid skeleton and pore fluid. The effects of porosity and viscosity in the case of the partial-open pore interface condition are similar to what was previously obtained in the fully open pore case. The present work could be extended to 2D and 3D cases, with the added consideration of shear waves. It would also be interesting to consider porous/fluid or porous/solid interfaces. The related problems are of great significance for the practical application of fluid-saturated porous phononic crystals and metamaterials.

Declaration of Competing Interest

The authors declare that they have no known competing financial interests or personal relationships that could have appeared to influence the work reported in this paper.

Acknowledgments

Financial supports by the National Natural Science Foundation of China (11702017, 11991031, 11991032, 12021002 and 11532001), the Young Elite Scientists Sponsorship Program by CAST (No. YESS20170022), and the EIPHI Graduate School (ANR-17-EURE-0002) are gratefully acknowledged.

Appendix A. Transfer matrices

The transfer matrices in Eqs. (17)–(19) are

$$\mathbf{P}_L^j = \begin{pmatrix} 1 & 1 & 1 & 1 \\ f_1^j & f_2^j & f_3^j & f_4^j \\ g_1^j & g_2^j & g_3^j & g_4^j \\ n_1^j & n_2^j & n_3^j & n_4^j \end{pmatrix},$$

$$\mathbf{Y} = \begin{pmatrix} 0 & 0 & 0 & 0 \\ 0 & 0 & 0 & 0 \\ 0 & 0 & 0 & 0 \\ f_1^2 & f_2^2 & f_3^2 & f_4^2 \end{pmatrix},$$

$$\mathbf{P}_R^j = \begin{pmatrix} \exp(iq_1^j x^{(j)}) & \exp(iq_2^j x^{(j)}) & \exp(iq_3^j x^{(j)}) & \exp(iq_4^j x^{(j)}) \\ f_1^j \exp(iq_1^j x^{(j)}) & f_2^j \exp(iq_2^j x^{(j)}) & f_3^j \exp(iq_3^j x^{(j)}) & f_4^j \exp(iq_4^j x^{(j)}) \\ g_1^j \exp(iq_1^j x^{(j)}) & g_2^j \exp(iq_2^j x^{(j)}) & g_3^j \exp(iq_3^j x^{(j)}) & g_4^j \exp(iq_4^j x^{(j)}) \\ n_1^j \exp(iq_1^j x^{(j)}) & n_2^j \exp(iq_2^j x^{(j)}) & n_3^j \exp(iq_3^j x^{(j)}) & n_4^j \exp(iq_4^j x^{(j)}) \end{pmatrix}, \quad (\text{A.1})$$

$$\mathbf{Z} = \begin{pmatrix} 0 & 0 & 0 & 0 \\ 0 & 0 & 0 & 0 \\ 0 & 0 & 0 & 0 \\ f_1^2 \exp(iq_1^2 a_2) & f_2^2 \exp(iq_2^2 a_2) & f_3^2 \exp(iq_3^2 a_2) & f_4^2 \exp(iq_4^2 a_2) \end{pmatrix}$$

Appendix B. Modal distribution

The coefficients used to calculate the modal distribution are

$$\mathbf{D} = (\mathbf{T} - \exp(ik_x a) \mathbf{I})(\mathbf{P}_R^2 + i\omega h \mathbf{Z})^{-1} \mathbf{P}_L^1,$$

$$\mathbf{E} = (\mathbf{P}_L^2 - i\omega h \mathbf{Y})^{-1} \mathbf{P}_R^1,$$

$$Q_1 = -\frac{(D_{34} D_{43} - D_{33} D_{44})(D_{44} D_{21} - D_{24} D_{41}) + (D_{44} D_{23} - D_{24} D_{43})(D_{31} D_{44} - D_{34} D_{41})}{(D_{34} D_{43} - D_{33} D_{44})(D_{44} D_{22} - D_{24} D_{42}) + (D_{44} D_{23} - D_{24} D_{43})(D_{32} D_{44} - D_{34} D_{42})},$$

$$R_1 = \frac{(D_{31} D_{44} - D_{34} D_{41}) + (D_{32} D_{44} - D_{34} D_{42}) Q_1}{D_{34} D_{43} - D_{33} D_{44}},$$

$$S_1 = -\frac{D_{41} + Q_1 D_{42} + R_1 D_{43}}{D_{44}},$$

$$O_2 = E_{11} + E_{12} Q_1 + E_{13} R_1 + E_{14} S_1,$$

$$Q_2 = E_{21} + E_{22} Q_1 + E_{23} R_1 + E_{24} S_1,$$

$$R_2 = E_{31} + E_{32} Q_1 + E_{33} R_1 + E_{34} S_1,$$

$$S_2 = E_{41} + E_{42} Q_1 + E_{43} R_1 + E_{44} S_1. \quad (\text{B.1})$$

Appendix C. Stiffness matrices

The matrices in Eq. (28) are expressed as

$$\mathbf{E}_{u1}^1 = \begin{pmatrix} 1 & 1 & 1 & 1 \\ f_2^1 & f_4^1 & f_1^1 & f_3^1 \\ \exp(iq_2^1 a_1) & \exp(iq_4^1 a_1) & \exp(iq_1^1 a_1) & \exp(iq_3^1 a_1) \\ f_2^1 \exp(iq_2^1 a_1) & f_4^1 \exp(iq_4^1 a_1) & f_1^1 \exp(iq_1^1 a_1) & f_3^1 \exp(iq_3^1 a_1) \end{pmatrix},$$

$$\mathbf{E}_{\sigma 1}^1 = \begin{pmatrix} g_2^1 & g_4^1 & g_1^1 & g_3^1 \\ n_2^1 & n_4^1 & n_1^1 & n_3^1 \\ g_2^1 \exp(iq_2^1 a_1) & g_4^1 \exp(iq_4^1 a_1) & g_1^1 \exp(iq_1^1 a_1) & g_3^1 \exp(iq_3^1 a_1) \\ n_2^1 \exp(iq_2^1 a_1) & n_4^1 \exp(iq_4^1 a_1) & n_1^1 \exp(iq_1^1 a_1) & n_3^1 \exp(iq_3^1 a_1) \end{pmatrix},$$

$$\mathbf{E}_{u2}^1 = \begin{pmatrix} 1 & 1 & 1 & 1 \\ f_2^2 & f_4^2 & f_1^2 & f_3^2 \\ \exp(iq_2^2 a_2) & \exp(iq_4^2 a_2) & \exp(iq_1^2 a_2) & \exp(iq_3^2 a_2) \\ f_2^2 \exp(iq_2^2 a_2) & f_4^2 \exp(iq_4^2 a_2) & f_1^2 \exp(iq_1^2 a_2) & f_3^2 \exp(iq_3^2 a_2) \end{pmatrix},$$

$$\mathbf{E}_{\sigma 2}^1 = \begin{pmatrix} g_2^2 & g_4^2 & g_1^2 & g_3^2 \\ n_2^2 - i\omega h f_2^2 & n_4^2 - i\omega h f_4^2 & n_1^2 - i\omega h f_1^2 & n_3^2 - i\omega h f_3^2 \\ g_2^2 \exp(iq_2^2 a_2) & g_4^2 \exp(iq_4^2 a_2) & g_1^2 \exp(iq_1^2 a_2) & g_3^2 \exp(iq_3^2 a_2) \\ n_2^2 \exp(iq_2^2 a_2) & n_4^2 \exp(iq_4^2 a_2) & n_1^2 \exp(iq_1^2 a_2) & n_3^2 \exp(iq_3^2 a_2) \end{pmatrix}, \quad (\text{C.1})$$

$$\mathbf{E}_{\sigma 1}^2 = \begin{pmatrix} g_2^1 & g_4^1 & g_1^1 & g_3^1 \\ n_2^1 - i\omega h f_2^1 & n_4^1 - i\omega h f_4^1 & n_1^1 - i\omega h f_1^1 & n_3^1 - i\omega h f_3^1 \\ g_2^1 \exp(iq_2^1 a_1) & g_4^1 \exp(iq_4^1 a_1) & g_1^1 \exp(iq_1^1 a_1) & g_3^1 \exp(iq_3^1 a_1) \\ n_2^1 \exp(iq_2^1 a_1) & n_4^1 \exp(iq_4^1 a_1) & n_1^1 \exp(iq_1^1 a_1) & n_3^1 \exp(iq_3^1 a_1) \end{pmatrix}$$

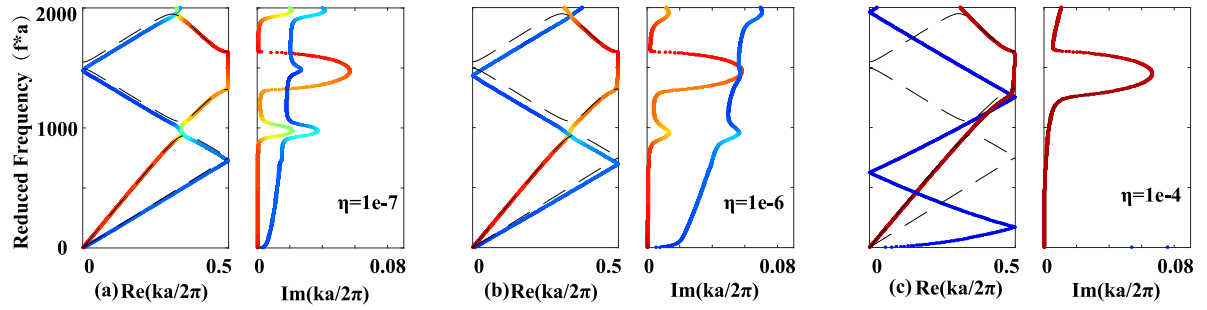


Fig. E.1. Influence of the fluid viscosity η (Pa-s) on the complex band structure for the 1D FSPPC with partial-open pore interfaces ($h = 10^5$ Pa-s/m). The dashed lines represent the results for lossless case ($\eta = 0$). All parameters except viscosity are the same as in Fig. 3.

Appendix D. Matrices elements

The elements of matrices \mathbf{M} , \mathbf{N}_{p2} and \mathbf{N}_{p1} are

$$\begin{aligned}
 M(1, 1) &= (K_N(1, 1) + K_N(1, 2)f_2^1 - g_2^1)\exp(iq_2^1 x_0), \\
 M(1, 2) &= (K_N(1, 1) + K_N(1, 2)f_4^1 - g_4^1)\exp(iq_4^1 x_0), \\
 M(1, 3) &= (K_N(1, 3) + K_N(1, 4)f_1^2)\exp(iq_1^2 x_s), \\
 M(1, 4) &= (K_N(1, 3) + K_N(1, 4)f_3^2)\exp(iq_3^2 x_s), \\
 M(2, 1) &= (K_N(2, 1) + K_N(2, 2)f_2^1 - n_2^1)\exp(iq_2^1 x_0), \\
 M(2, 2) &= (K_N(2, 1) + K_N(2, 2)f_4^1 - n_4^1)\exp(iq_4^1 x_0), \\
 M(2, 3) &= (K_N(2, 3) + K_N(2, 4)f_1^2)\exp(iq_1^2 x_s), \\
 M(2, 4) &= (K_N(2, 3) + K_N(2, 4)f_3^2)\exp(iq_3^2 x_s), \\
 M(3, 1) &= (K_N(3, 1) + K_N(3, 2)f_2^1)\exp(iq_2^1 x_0), \\
 M(3, 2) &= (K_N(3, 1) + K_N(3, 2)f_4^1)\exp(iq_4^1 x_0), \\
 M(3, 3) &= (K_N(3, 3) + K_N(3, 4)f_1^2 - g_1^2)\exp(iq_1^2 x_s), \\
 M(3, 4) &= (K_N(3, 3) + K_N(3, 4)f_3^2 - g_3^2)\exp(iq_3^2 x_s), \\
 M(4, 1) &= (K_N(4, 1) + K_N(4, 2)f_2^1)\exp(iq_2^1 x_0), \\
 M(4, 2) &= (K_N(4, 1) + K_N(4, 2)f_4^1)\exp(iq_4^1 x_0), \\
 M(4, 3) &= (K_N(4, 3) + K_N(4, 4)f_1^2 - n_1^2)\exp(iq_1^2 x_s), \\
 M(4, 4) &= (K_N(4, 3) + K_N(4, 4)f_3^2 - n_3^2)\exp(iq_3^2 x_s),
 \end{aligned} \tag{D.1}$$

$$\begin{aligned}
 N_{p2}(1, 1) &= -(K_N(1, 1) + K_N(1, 2)f_1^1 - g_1^1)\exp(iq_1^1 x_0), \\
 N_{p2}(2, 1) &= -(K_N(2, 1) + K_N(2, 2)f_1^1 - n_1^1)\exp(iq_1^1 x_0), \\
 N_{p2}(3, 1) &= -(K_N(3, 1) + K_N(3, 2)f_1^1)\exp(iq_1^1 x_0), \\
 N_{p2}(4, 1) &= -(K_N(4, 1) + K_N(4, 2)f_1^1)\exp(iq_1^1 x_0), \\
 N_{p1}(1, 1) &= -(K_N(1, 1) + K_N(1, 2)f_3^1 - g_3^1)\exp(iq_3^1 x_0), \\
 N_{p1}(2, 1) &= -(K_N(2, 1) + K_N(2, 2)f_3^1 - n_3^1)\exp(iq_3^1 x_0), \\
 N_{p1}(3, 1) &= -(K_N(3, 1) + K_N(3, 2)f_3^1)\exp(iq_3^1 x_0), \\
 N_{p1}(4, 1) &= -(K_N(4, 1) + K_N(4, 2)f_3^1)\exp(iq_3^1 x_0).
 \end{aligned} \tag{D.2}$$

Appendix E. Fluid viscosity

The effect of the fluid viscosity coefficient (η) on the complex band structure for the 1D FSPPC with the partial-open pore interface is shown in Fig. E.1.

References

- [1] Kushwaha MS, Halevi P, Dobrzynski L, Djafari-Rouhani B. Acoustic band structure of periodic elastic composites. *Phys Rev Lett* 1993;71:2022–5.
- [2] Tamura S, Hurley DC, Wolfe JP. Acoustic-phonon propagation in superlattices. *Phys Rev B* 1988;38:1427–49.
- [3] Mizuno S. Resonance and mode conversion of phonons scattered by superlattices with inhomogeneity. *Phys Rev B* 2003;68:193305.

- [4] Liu Z, Zhang X, Mao Y, Zhu YY, Yang Z, Chan CT, Ping S. Locally resonant sonic materials. *Science* 2000;338:201–5.
- [5] Page JH, Yang S, Liu Z, Cowan ML, Chan CT, Sheng P. Tunneling and dispersion in 3D phononic crystals. *Ztschrift fur Kristallographie* 2005;220:859–70.
- [6] Huang HH, Sun CT, Huang GL. On the negative effective mass density in acoustic metamaterials. *Int J Eng Sci* 2009;47:610–17.
- [7] Zhu R, Liu XN, Huang GL, Huang HH, Sun CT. Microstructural design and experimental validation of elastic metamaterial plates with anisotropic mass density. *Phys Rev B* 2012;86:144307.
- [8] Safavi-Naeini AH, Painter O. Design of optomechanical cavities and waveguides on a simultaneous bandgap phononic-photon crystal slab. *Optics Express* 2010;18:014926.
- [9] Wang YF, Wang TT, Liu JP, Wang YS, Laude V. Guiding and splitting lamb waves in coupled-resonator elastic waveguides. *Compos Struct* 2018;206:588–93.
- [10] Zhu R, Liu XN, Hu GK, Sun CT, Huang GL. Negative refraction of elastic waves at the deep-subwavelength scale in a single-phase metamaterial. *Nat Commun* 2014;5:5510.
- [11] Luo C, Johnson SG, Joannopoulos JD, Pendry JB. All-angle negative refraction without negative effective index. *Phys Rev B* 2002;65:201104.
- [12] Lin S-CS, Huang TJ, Sun JH, Wu TT. Gradient-index phononic crystals. *Phys Rev B* 2009;79:288–93.
- [13] Zhao J, Bonello B, Marchal R, Boyko O. Beam path and focusing of flexural lamb waves within phononic crystal-based acoustic lenses. *N J Phys* 2014;16:063031.
- [14] Wang YF, Wang YZ, Wu B, Chen W, Wang YS. Tunable and active phononic crystals and metamaterials. *Appl Mech Rev* 2020;72:040801.
- [15] Li FL, Wang YS, Zhang C, Yu GL. Bandgaps of two-dimensional phononic crystals with sliding interface conditions. *J Appl Mech* 2014;81:064501.
- [16] Li FL, Wang YS, Zhang C. A BEM for band structure and elastic wave transmission analysis of 2D phononic crystals with different interface conditions. *Int J Mech Sci* 2018;144:110–17.
- [17] Albuquerque EL, Sesion PD. Band gaps of acoustic waves propagating in a solid/liquid phononic Fibonacci structure. *Physica B Condens Matter* 2010;405:3704–8.
- [18] Xu YL, Tian XG, Chen CQ. Band structures of two dimensional solid/air hierarchical phononic crystals. *Physica B Condens Matter* 2012;407:1995–2001.
- [19] Wang TT, Wang YF, Wang YS, Laude V. Tunable fluid-filled phononic metastrap. *Appl Phys Lett* 2017;111:041906.
- [20] WeeRazip MFM, Addouche M, Siow KS, Zain ARM, Elayouch A, Chollet F, et al. Guiding and confinement of interface acoustic waves in solid-fluid pillar-based phononic crystals. *AIP Adv* 2016;6:1–9.
- [21] Zhen N, Wang YS. Surface effects on bandgaps of transverse waves propagating in two dimensional phononic crystals with nanosized holes. *Mater Sci Forum* 2011;675-677:611–14.
- [22] Zhen N, Wang YS, Zhang C. Surface/interface effect on band structures of nanosized phononic crystals. *Mech Res Commun* 2012;46:81–9.
- [23] Alevizaki A, Sainidou R, Rembert P, Morvan B, Stefanou N. Phononic crystals of poroelastic spheres. *Phys Rev B* 2016;94:174306.
- [24] Jiang C, Huang L. Realization of equivalent gradient of porous materials with periodic macro void structure. *Mech Syst Signal Process* 2020;136:106434.
- [25] Zhu XF, Lau SK, Lu Z, Jeon W. Broadband low-frequency sound absorption by periodic metamaterial resonators embedded in a porous layer. *J Sound Vib* 2019;461:114922.
- [26] Wang YF, Liang JW, Chen AL, Wang YS, Laude V. Wave propagation in one-dimensional fluid-saturated porous metamaterials. *Phys Rev B* 2019;99:134304.
- [27] Wang YF, Liang JW, Chen AL, Wang YS, Laude V. Evanescent waves in two-dimensional fluid-saturated porous metamaterials with a transversely isotropic matrix. *Phys Rev B* 2020;101:184301.
- [28] Meng LK, Cheng ZB, Shi ZF. Vibration mitigation in saturated soil by periodic pile barriers. *Comput Geotech* 2020;117:103251.
- [29] Meng LK, Cheng ZB, Shi ZF. Vibration mitigation in saturated soil by periodic infilled pipe pile barriers. *Comput Geotech* 2020;124:103633.
- [30] Meng QJ, Shi ZF. Vibration isolation of plane waves by periodic pipe pile barriers in saturated soil. *J Aerosp Eng* 2019;32:04018114.
- [31] Geertsma J, Smit DC. Some aspects of elastic wave propagation in fluid-saturated porous solids. *Geophysics* 1961;26:169–81.

- [32] Lovera OM. Boundary conditions for fluid-saturated porous solid. *Geophysics* 1987;52:174–8.
- [33] Rasolofosaon PNJ. Importance of interface hydraulic condition on the generation of second bulk compressional wave in porous media. *Appl Phys Lett* 1988;52:780–2.
- [34] Wu KY, Xue Q, Laszlo A. Reflection and transmission of elastic waves from a fluid-saturated porous solid boundary. *J Acoust Soc Am* 1990;87:2349–58.
- [35] Denneman AIM, Drijkoningen GG, Smeulders DMJ, Wapenaar K. Reflection and transmission of waves at a fluid/porous-medium interface. *Geophysics* 2001;67:282–91.
- [36] Vashisth AK, Sharma MD, Gogna ML. Reflection and transmission of elastic waves at a loosely bonded interface between an elastic solid and liquid-saturated porous solid. *Geophys J R Astron Soc* 1991;105:601–17.
- [37] Vashisth AK, Gogna ML. The effect of loose boundaries on wave propagation in a porous solid: reflection and refraction of seismic waves across a plane interface. *Int J Solids Struct* 1993;30:2485–99.
- [38] Deresiewicz H, Skalak R. On uniqueness in dynamic poroelasticity. *Bull Seismol Soc Am* 1963;53:783–8.
- [39] Kumar R, Miglani A. Effect of pore alignment on surface wave propagation in a liquid-saturated porous layer over a liquid-saturated porous half-space with loosely bonded interface. *J Phys Earth* 1996;44:153–72.
- [40] Sharma MD. Wave propagation across the boundary between two dissimilar poroelastic solids. *J Sound Vibr* 2008;314:657–71.
- [41] Biot MA. Theory of propagation of elastic waves in a fluid-saturated porous solid: II. Higher frequency range. *J Acoust Soc Am* 1956;28:168–78.
- [42] Kazi-Aoual MN, Bonnet G, Jouanna P. Green's functions in an infinite transversely isotropic saturated poroelastic medium. *J Acoust Soc Am* 1988;84:1883–9.
- [43] de Boer R. Highlights in the historical development of the porous media theory: toward a consistent macroscopic theory. *Appl Mech Rev* 1996;49:201–62.
- [44] Nayfeh AH. Wave propagation in layered anisotropic media with applications to composites. *J Acoust Soc Am* 2000;108:471–2.
- [45] Rokhlin SI, Wang L. Stable recursive algorithm for elastic wave propagation in layered anisotropic media: Stiffness matrix method. *J Acoust Soc Am* 2002;112:822–34.
- [46] Pastureaud T, Laude V, Ballandras S. Stable scattering-matrix method for surface acoustic waves in piezoelectric multilayers. *Appl Phys Lett* 2002;80:2544–6.
- [47] Reinhardt A, Pastureaud T, Ballandras S, Laude V. Scattering matrix method for modeling acoustic waves in piezoelectric, fluid, and metallic multilayers. *J Appl Phys* 2003;94:6923–31.
- [48] Yan DJ, Chen AL, Wang YS, Zhang C, Golub M. In-plane elastic wave propagation in nanoscale periodic layered piezoelectric structures. *Int J Mech Sci* 2018;142-143:276–88.